Check for updates

Advanced Materials

ADVANCED MATERIALS
www.advmat.de

RESEARCH ARTICLE

Interconnected Closed Pores Enable Dense and Facile Sodium Storage in Hard Carbon

Guobiao Jin[1] | Chang Wang[1] | Feng Jin[1] | Rui Liu[1] | Xinlin Shi[1] | Hongpeng Liu[2] | Junping Jia[3] | Peng Du[2] | Zirui Lou[1] | Feng Pan[1]

[1]School of Advanced Materials, Peking University, Shenzhen Graduate School, Shenzhen, P. R. China | [2]K. H. Kuo Center for Material Characterization, Liaoning Academy of Materials, Shenyang, Liaoning, P. R. China | [3]College of Materials Science and Engineering, Shenzhen University, Shenzhen, P. R. China

Correspondence: Feng Jin (jin.feng@pku.edu.cn) | Zirui Lou (zrlou@pku.edu.cn) | Feng Pan (panfeng@pkusz.edu.cn)

Received: 2 April 2026 | **Revised:** 26 June 2026 | **Accepted:** 21 July 2026

Keywords: hard carbons | interconnected closed pores | plateau capacities | sodium–ion batteries

ABSTRACT

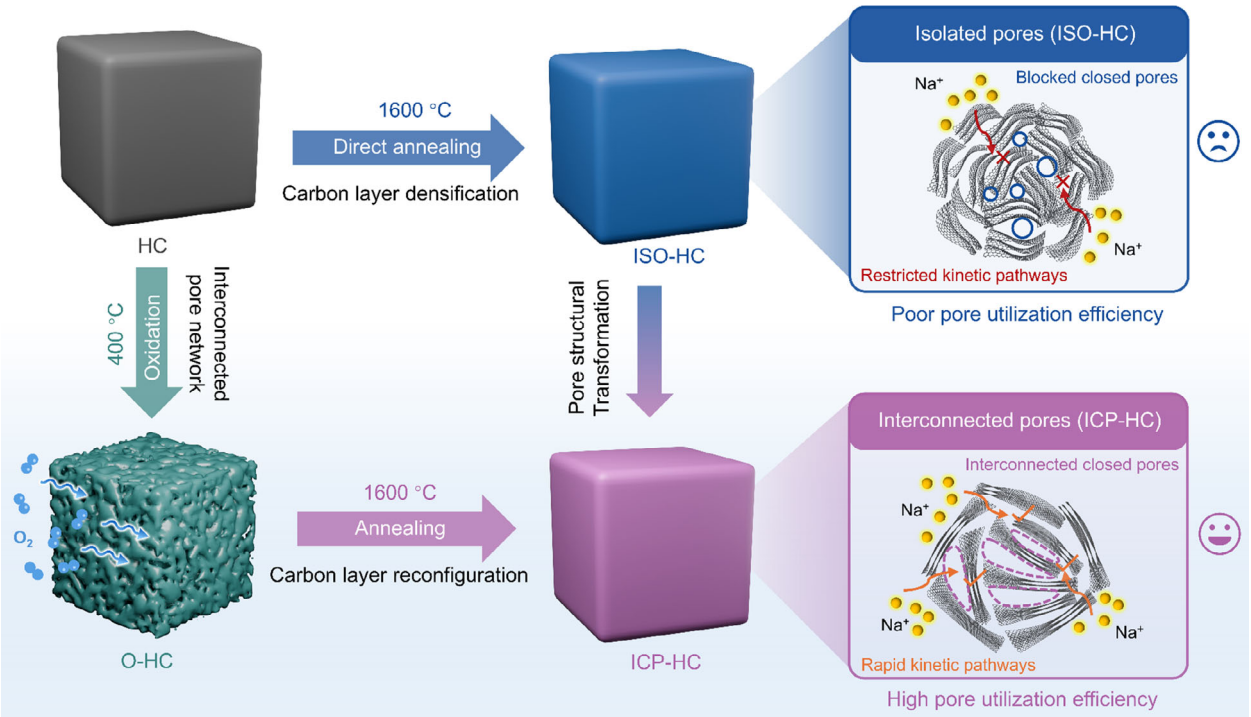
Achieving a high plateau capacity in hard carbon (HC) anodes is one of the most critical prerequisites for high-energy-density sodium–ion batteries (SIBs), yet it is fundamentally limited by inaccessible closed pores formed during conventional high-temperature annealing. Here, we propose a potentially scalable oxidation-reconfiguration strategy to unlock its latent capacity. By coupling controlled oxidative etching with subsequent thermal reconstruction, an interconnected closed-pore network is constructed. Oxidative pretreatment opens blocked channels and interconnects isolated voids, while reconstruction promotes void fusion, generating accessible internal reservoirs for the nucleation and storage of quasi-metallic sodium clusters. This structural evolution and storage mechanism are elucidated by total neutron scattering, SAXS, in situ techniques, and simulations. As a result, the optimized ICP-HC anode delivers reversible capacity 437 mAh g^{-1} with an initial Coulombic efficiency of 91.5%. It achieves an initial discharge plateau capacity of 399 mAh g^{-1} with fast kinetics (300 mAh g^{-1} at 2C), overcoming the capacity-rate trade-off. Furthermore, an NVP//ICP-HC full cell shows excellent rate capability (96 mAh g^{-1} at 5C) and stable cycling (95% retention over 200 cycles at 1C). This work provides a scalable strategy for advanced carbon anodes in high-energy-density SIBs.

1 | Introduction

Driven by the abundance of raw materials and cost-effectiveness, sodium–ion batteries (SIBs) are widely regarded as promising candidates for grid-scale energy storage [1–3]. Among various anode materials, hard carbon (HC) stands out due to its competitive specific capacity, structural stability, and ideal compatibility with sodium chemistry [4, 5]. Structurally, HC is a non-graphitizable carbon consisting of turbostratic layers, graphitic nanodomains, and internal nanopores [6, 7]. Electrochemically, its sodium storage profile typically consists of a high-voltage sloping region and a low-voltage plateau region, corresponding to surface-defect adsorption and bulk insertion/pore-filling mechanisms, respectively [8, 9]. Because the plateau region delivers capacity at a potential close to that of sodium metal, maximizing this low-voltage contribution is the most crucial prerequisite for achieving high-energy-density SIBs [10–13]. However, conventional hard carbons generally suffer from an excessive sloping capacity or an insufficient plateau region, severely constraining their practical energy density.

According to the widely accepted pore-filling mechanism [14–16], the massive plateau capacity originates predominantly from the dense accommodation of quasi-metallic sodium clusters within the internal closed micropores. Principally, unlocking ultra-high plateau capacity requires a massive volume of sodium-accessible closed pores. To construct such architectures, conventional strategies heavily rely on bottom-up precursor engineering, introducing

All rights reserved, including rights for text and data mining and training of artificial intelligence technologies or similar technologies.
© 2026 Wiley-VCH GmbH



SCHEME 1 | Schematic illustration of the material synthesis and structural evolution mechanisms. Comparison between the conventional direct annealing route (top) and the proposed oxidation strategy (bottom).

chemical activators or templating agents (e.g., ZnO, $ZnAc_2$, MgO, KOH, and so forth [17–22].) into raw carbon precursors prior to pyrolysis to generate more closed pores in hard carbon. However, these precursor-dependent strategies typically involve complex, multi-step synthetic procedures and tedious washing processes, which severely hinder their scalable commercialization. Alternatively, for readily available hard carbons, directly elevating the carbonization temperature is a more facile and scalable approach to heal surface defects, enrich the closed-pore volume, and thereby improve the initial Coulombic efficiency (ICE) [23–25]. However, a critical structural dilemma emerges at ultra-high temperatures: while extreme thermal treatment promotes closed-pore formation, it concurrently induces extensive graphitization and lattice densification [26–28]. This severe structural shrinkage irreversibly pinches off the ion diffusion pathways connecting the external environment to the internal voids. Consequently, a vast number of these internal pores are transformed into electrochemically inactive dead pores that are entirely inaccessible to sodium ions. This restricted internal accessibility not only leads to a pronounced degradation in overall capacity, but also inherently triggers sluggish ion diffusion kinetics [27–30].

To fundamentally overcome this permeability-capacity trade-off, we propose a scalable oxidation-reconfiguration strategy to unlock the latent plateau capacity of hard carbons. This meticulously designed two-step process involves a controlled oxidative etching at a critical thermodynamic threshold (400°C, the critical temperature just before HC combustion, Figure S1) to selectively remove highly disordered domains and open originally blocked micropores, creating an interconnected pore network, followed by a high-temperature annealing step (1600°C) for carbon layers rearrangement to achieve closed-pore structural reconfiguration (Scheme 1). The defects and open channels introduced during the initial oxidation act as structural directors, effectively lowering the energy barrier for graphitization during the subsequent annealing. Unlike direct high-temperature annealing, which isolates pores and blocks ion diffusion channel, this unique synergistic strategy drives the coalescence of small, dispersed voids into expanded, interconnected closed pores while successfully preserving the highly interconnected ion-diffusion network. This architecturally optimized hard carbon with interconnected closed-pore (denoted as ICP-HC) not only effectively shields the co-intercalation of electrolyte solvent molecules to ensure high initial reversibility but also provides abundant accessible internal volume for sodium cluster nucleation. As a result, ICP-HC exhibits a remarkable reversible capacity of 437 mAh g^{-1} with a high ICE of 91.5%. Most notably, it delivers an ultra-high discharge plateau capacity of 399 mAh g^{-1}. The practical viability of this material is further validated in a full-cell configuration paired with a $Na_3V_2(PO_4)_3$ (NVP) cathode, yielding excellent high-rate performance (96 mAh g^{-1} at 5C based on NVP) and durable cycling stability (95% capacity retention over 200 cycles at 1C). This work provides deep insights into the correlation between internal pore interconnectivity and microscopic electrochemical kinetics, offering a highly practical pathway for the precise structural engineering of next-generation ultra-high-capacity hard carbon anodes.

2 | Results and Discussion

2.1 | Chemical and Microstructural Evolution of Hard Carbon

To evaluate the effect of O_2 and high-temperature annealing, comprehensive physiochemical techniques were employed, including

15214095, 0, Downloaded from https://advanced.onlinelibrary.wiley.com/doi/10.1002/adma.74503 by University Town Of Shenzhen, Wiley Online Library on [08/09/2026]. See the Terms and Conditions (https://onlinelibrary.wiley.com/terms-and-conditions) on Wiley Online Library for rules of use; OA articles are governed by the applicable Creative Commons License

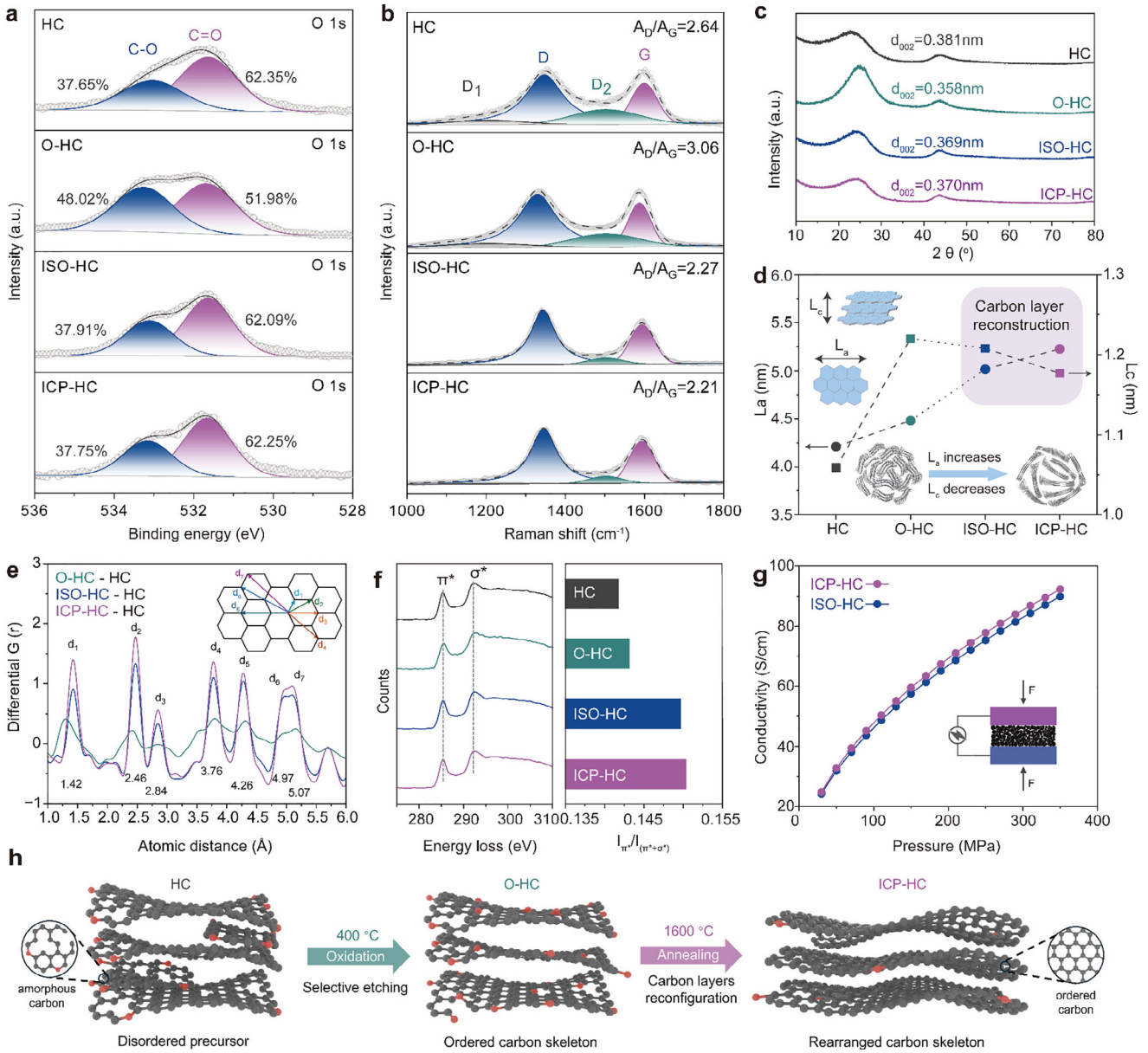


FIGURE 1 | Structural characterization of the hard carbons. (a) High-resolution XPS O 1s spectra. (b) Raman spectra with calculated ratios. (c) XRD patterns. (d) The corresponding evolution of microcrystalline parameters derived from peak fitting. (e) Differential neutron pair distribution function (DNPDF) curves revealing the local atomic coordination. (f) Electron energy loss spectroscopy (EELS) of the carbon K-edge (left) and the corresponding quantitative ratio of (right), reflecting the hybridization content. (g) Pressure-dependent electronic conductivity of ICP-HC and ISO-HC powders. (h) Illustration of structural evolution of the carbon skeleton.

Scanning electron microscopy (SEM), X-ray photoelectron spectroscopy (XPS), Raman spectroscopy, X-ray diffraction (XRD), Neutron Pair Distribution Function (NPDF), electron energy loss spectroscopy (EELS).

SEM images reveal that no obvious morphology changes observed for all the treated HCs (O-HC, ISO-HC, and ICP-HC), with retaining the irregular block-like morphology of pristine HC, suggesting that neither the low-temperature oxidation nor the high-temperature annealing significantly alters the macroscopic texture of the hard carbon particles (Figure S2). High-resolution XPS O 1s spectra (Figure 1a) shows that C—O bond locating at ~533.0 eV and total oxygen content, increased to 48.02% and 4.04% in O-HC, proving the graft of oxygen functionalities after O_2 treatment (Figures S3 and S4; Table S1). And the area ratio of *D*-band (1350 cm^{-1}) and *G*-band (1580 cm^{-1}) in Raman spectroscopy, denoted as A_D/A_G, increased significantly from 2.64 (HC) to 3.06 (O-HC) signaling a rise in lattice disorder, which indicates O_2 acts as a defect-activator (Figure 1b; Tables S2 and S3). Furthermore, the diffraction peak at ~23° in XRD patterns (Figure 1c), assigned to (002) peak, shift to higher angle, accompanied by lateral crystallite size increase, which implies a preferential etching mechanism, where oxygen selectively consumed the highly unstable, high-energy amorphous carbon regions, leaving behind a relatively ordered carbon skeleton (Figure S6).

Subsequent annealing at 1600°C (yielding ICP-HC) effectively eliminated these metastable oxygen species after oxygen

15214095, 0, Downloaded from https://advanced.onlinelibrary.wiley.com/doi/10.1002/adma.74503 by University Town Of Shenzhen, Wiley Online Library on [08/09/2026]. See the Terms and Conditions (https://onlinelibrary.wiley.com/terms-and-conditions) on Wiley Online Library for rules of use; OA articles are governed by the applicable Creative Commons License

treatment, achieving a deoxygenated surface state like the directly annealed counterpart (ISO-HC). Crucially, this oxidation strategy proved superior to direct annealing in optimizing the carbon lattice. TheA_D/A_G ratio of ICP-HC decreased dramatically to 2.21, which is lower than that of ISO-HC (2.27) (Figures 1b and S5), suggesting that the defects created by oxidation effectively lowered the energy barrier for graphitization, facilitating an ordering process. XRD results further highlight it: unlike ISO-HC, showing a normal graphitization shift to higher angles, ICP-HC exhibits a distinct shift of the (002) peak to a lower angle with a broadened FWHM compared to O-HC (Figures 1c and S6). Fitted parameters further reveal that ICP-HC possesses a longer L_a but smaller L_c compared to ISO-HC, hinting at the formation of expanded, fused voids within the turbostratic domains (Figure 1d and Table S4).

This structural enhancement is further corroborated by Neutron Pair Distribution Function (NPDF) analysis and Electron Energy Loss Spectroscopy (EELS). NPDF analysis (Figure 1e; Figures S7 and S8) confirms that the local atomic coordination remains robust, with sharp peaks at 1.42 Å (nearest-neighbor C-C), 2.46 Å (second-neighbor in-plane distance), and 2.84 Å (inter-layer distance). Notably, the intensity of these peaks increased slightly after oxidation and further intensified after reconfiguration (ICP-HC > ISO-HC), evidencing a robust restoration of short-range ordering and the formation of a coherent carbon lattice. The EELS spectra (Figure 1f and Table S5) display characteristic peaks at ~285 and ~292 eV, attributed to sp^2 and sp^3 hybridization, respectively. ICP-HC exhibits the highest intensity ratio of $I_{\pi*}/I_{(\pi*+\sigma*)}$, an indicative for degree of graphitization, indicating a maximized-hybridized carbon content and the formation of an extended delocalized-electron system. Bridging the microscopic ordering with macroscopic performance, pressure-dependent conductivity measurements demonstrate that ICP-HC possesses superior macroscopic electronic conductivity across the entire pressure range (Figure 1g). As schematically illustrated in Figure 1h, the oxidation-reconfiguration strategy fundamentally transforms the initial turbostratic matrix. Consistent with the previously observed increases in L_a and graphitization degree, the selective elimination of disordered domains leaves behind intact, highly effective electron transport channels. Consequently, this intrinsically optimized carbon framework maintains exceptional conductivity, establishing a robust physical foundation and the necessary electronic transmission channel for high-performance, high-rate SIBs.

2.2 | Evolution of Pore Architecture

The evolutions of the pore architecture were systematically tracked via gas absorption isotherms, small-angle X-ray scattering (SAXS), and high-resolution transmission electron microscopy (HRTEM). Figure 2a displays the N_2 adsorption-desorption isotherms. Pristine HC exhibits a non-porous nature with negligible N_2 adsorption. Upon oxidation, the O-HC sample transforms into a highly porous architecture with a typical Type-I isotherm [31, 32], confirming that the oxidative etching selectively removes disordered carbon domains and effectively unlocks the originally blocked micropores. Subsequently, following high-temperature annealing, the N_2 uptake of ICP-HC drops precipitously to a level comparable to that of the directly annealed ISO-HC. This drastic reduction demonstrates that the thermally driven carbon layers rearrangement promotes the re-closure of surface openings, effectively isolating the internal voids from the external environment. Despite this surface closure, the internal pore structure of ICP-HC differs fundamentally from that of ISO-HC. As revealed by the CO_2 adsorption isotherms (Figure 2b), ICP-HC retains a significantly higher adsorption capacity than ISO-HC. Pore size distribution analysis (Figure 2c) further clarifies that this enhanced capacity stems from a massive abundance of ultra-micropores (0.4–0.8 nm). Collectively, these results clearly demonstrate that the oxidation-reconfiguration process not only expands the internal volume of the closed-pore architecture but also successfully unlocks their accessibility, allowing probe molecules and subsequently sodium ions to readily penetrate the carbon framework.

To probe the evolution of closed pores, SAXS analysis and ab initio 3D shape reconstruction was performed based on the SAXS profiles. The scattering intensity in the low-q region (q = 0.5~1 nm^{-1}) increases significantly due to oxidation (Figure 2d), an indicative of enlarged pores with oxygen treatment. Such behaviors provide strong evidence for the precise etching of disordered carbon species by oxygen, perfectly aligning with the previously discussed structural evolution where the carbon lattice exhibits enhanced short-range ordering following the oxygen treatment. Upon high-temperature annealing, the low-q region scattering intensity of ICP-HC further intensifies compared to ISO-HC, and the pair distance distribution function P(r) peak shifts toward a larger radius and the peak shifts to even larger radii compared to ISO-HC, serving as compelling evidence for pore expansion. By fitting the high-q scattering regions (q = 3~6 nm^{-1}) according to the Porod power-law equation ($I(q) \propto q^{-D_p}$) [33], the Porod exponents (D_p) were extracted to assess the interfacial roughness (Figures 2e and S9). The obtained D_p values for HC, O-HC, ISO-HC, and ICP-HC are 2.33, 3.09, 2.81, and 2.87, respectively. All these values are strictly below 4, confirming that the internal pores possess distinct fractal characteristics with rough interfaces rather than ideal sharp boundaries [34, 35]. While the final high-temperature annealing process reconstructs the pore walls and yields comparable interfacial roughness for both ICP-HC and ISO-HC, their global pore network connectivity exhibits a stark contrast. To compare this macroscopic interconnectivity, the amphiphilic factor (f_a) was calculated (Figure 2e and Table S8), where a larger f_a value theoretically signifies a more disordered and highly interconnected pore network [36]. Direct high-temperature annealing severely limits the extension of the pores, resulting in a significantly depressed f_a value of 0.186 for the control ISO-HC. This low value is highly indicative of structural shrinkage and the formation of isolated, inaccessible voids. In striking contrast, the engineered ICP-HC maintains a remarkably high f_a value of 0.559, which perfectly inherits the highly penetrated network created during the preceding oxidation stage (O-HC, f_a = 0.563). Furthermore, ab initio 3D shape reconstruction visually validates this topology [37–40], unlike the ISO-HC, the ICP-HC model displays distinct volumetric expansion with fused internal voids (Figures 2f and S10), thereby verifying a substantial improvement in the pore network interconnectivity. Collectively, this structural synergy unequivocally demonstrates that the oxidation-reconfiguration strategy not only constructs stable fractal pore interfaces but, fundamentally, prevents the detrimental isolation of closed pores, realizing an internally interconnected

15214095, 0, Downloaded from https://advanced.onlinelibrary.wiley.com/doi/10.1002/adma.74503 by University Town Of Shenzhen, Wiley Online Library on [08/09/2026]. See the Terms and Conditions (https://onlinelibrary.wiley.com/terms-and-conditions) on Wiley Online Library for rules of use; OA articles are governed by the applicable Creative Commons License

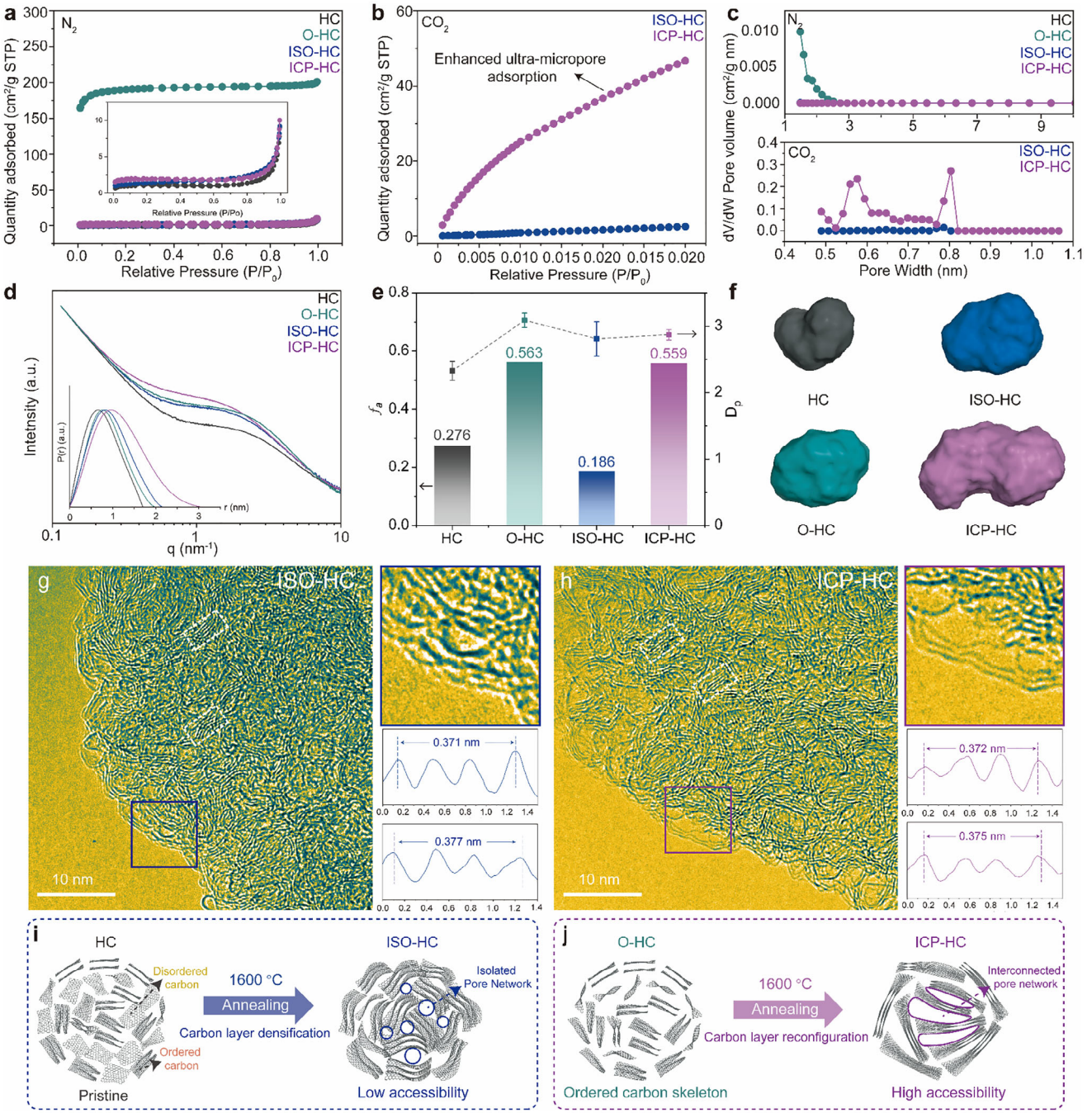


FIGURE 2 | Evolution of pore architecture. (a) N_2 adsorption–desorption isotherms at 77 K. (b) CO_2 adsorption isotherms at 273 K. (c) Pore size distributions calculated using the DFT model. (d) SAXS profiles and pair distance distribution functions derived from SAXS data. (e) Evolution of the amphiphilic factor (f_a) and Porod fractal dimensions, illustrating the degree of pore interconnectivity/disorder and interfacial roughness, respectively. (f) Ab initio 3D shape reconstructions of the scattering bodies (pores) for HC, O-HC, ISO-HC, and ICP-HC, visually demonstrating volumetric expansion and pore interconnection. High-resolution TEM (HRTEM) images with corresponding line intensity profiles (insets) for (g) ISO-HC and (h) ICP-HC, revealing the distinct local graphitic stacking and closed-pore morphology. (i, j) Schematic illustration of the divergent pore structure evolution mechanisms.

closed-pore network. HRTEM imaging further corroborates this structural optimization. As shown in Figures 2g and S11, ISO-HC exhibits a densely packed house-of-cards microstructure with short, highly tortuous graphene layers. These sparse and narrow voids severely restrict the space available for sodium cluster nucleation. Conversely, driven by the oxidation-reconfiguration process, ICP-HC (Figure 2h) displays significantly enhanced continuity and extended graphitic fringes. Crucially, interconnected closed nanopores encapsulated by continuous, curved graphene-like shells are clearly observed. These enlarged pores, originating from micropore coalescence, provide ample reservoirs for quasi-metallic sodium storage, perfectly matching the expanded pore size evidenced by SAXS. Furthermore, Figure 2i,j elucidates the underlying reconstruction mechanism. While conventional

15214095, 0, Downloaded from https://advanced.onlinelibrary.wiley.com/doi/10.1002/adma.74503 by University Town Of Shenzhen, Wiley Online Library on [08/09/2026]. See the Terms and Conditions (https://onlinelibrary.wiley.com/terms-and-conditions) on Wiley Online Library for rules of use; OA articles are governed by the applicable Creative Commons License

annealing causes severe densification and pore isolation (ISO-HC), oxidation-reconfiguration selectively removes amorphous bottlenecks. This targeted pruning drives the carbon layers to rearrange and fuse into an interconnected closed-pore network (ICP-HC), successfully unlocking dead pores to drive high-performance sodium storage. Collectively, this structural synergy demonstrates that our strategy fundamentally prevents closed-pore isolation. This highly accessible architecture ensures rapid sodium–ion transport kinetics and massive sodium cluster accommodation, thereby maximizing the overall pore utilization efficiency.

2.3 | Electrochemical Sodium-Storage Performance

The sodium storage behaviors of the hard carbon anodes were evaluated via half-cell with the configuration of Na | HC. Galvanostatic charge-discharge curves for HC and O-HC show that HC-based cells exhibit typical hard carbon behavior with mixed slope and plateau capacities, while cells with O-HC display a slope-dominated curve (Figure S12). This distinctive behavior confirms that the low-temperature oxidation introduces abundant surface defects and unlocks closed-pores, which enhance surface adsorption (slope region) and disrupt the closed-pore structure essential for plateau sodium storage. After annealing, both ISO-HC and ICP-HC exhibit two distinct characteristic regions: a sloping region and a plateau region. The optimized ICP-HC anode delivers a remarkable reversible specific capacity of 437 mAh g^{-1} with high initial Coulombic efficiency (ICE) of 91.5%, significantly outperforming the ISO-HC sample (300 mAh g^{-1} and 90.3%, respectively) (Figure 3a; Figures S13 and S14). Notably, Using 0.15 V versus Na/Na^+ as the boundary between the sloping and plateau regions [17, 18, 41], ICP-HC delivers an ultra-high discharge plateau capacity of 399 mAh g^{-1}, representing a substantial increase of ~157 mAh g^{-1} over ISO-HC, with similar slope capacity, originating from the interconnected closed pores, which serve as primary reservoirs for dense sodium clustering. To verify the effect of oxidative etching, the differential capacity (d_Q/d_V) plots display that ICP-HC possesses a lower average plateau potential compared to ISO-HC, a feature critical for maximizing the energy density of full batteries (Figure 3b).

To systematically elucidate the sodium storage kinetics, galvanostatic intermittent titration technique (GITT) and variable-rate cyclic voltammetry (CV) measurements were conducted. Based on the GITT profiles, the calculated sodium ion diffusion coefficients (D_{Na+}) reveal distinct kinetic behaviors across the slope and plateau regions (Figure 3c). Notably, ICP-HC displays a significantly elevated D_{Na+} in the slope region, reflecting its accelerated sodium adsorption kinetics. Moreover, the potential at which D_{Na+} reaches its local minimum representing the kinetic bottleneck of sodium diffusion is significantly delayed to a lower potential for ICP-HC (0.0139 V) compared to ISO-HC (0.0433 V). This downward shift indicates smoother mass transport and reduced diffusion resistance at the deep sodiation stage. CV curves recorded at varying scan rates from 0.2 to 1.2 mV s^{-1} further support the improved kinetic response of ICP-HC (Figure S15). Compared with ISO-HC, ICP-HC exhibits higher peak current and a larger apparent capacitive contribution derived from CV current separation, indicating a greater fast-response (Figure 3d) [41–47]. Collectively, these findings demonstrate that the oxidation-reconfiguration strategy effectively enhances ion accessibility within the interconnected closed pores, providing abundant active sites for pseudo-capacitive storage and facilitating rapid bulk ion diffusion, thereby ensuring superior overall rate kinetics. Benefiting from these kinetic advantages, the ICP-HC anode exhibits exceptional rate capability (Figures 3e and S16). ICP-HC-based cells deliver higher reversible capacities than ISO-HC at all rates. Furthermore, long-term cycling tests demonstrate the superiority of ICP-HC with retaining 93% of its initial capacity after 120 cycles at 0.1 C (Figure 3f) and 93% retention after150 cycles at 2 C current density (Figure S17).

To evaluate the full-cell applicability of ICP-HC, sodium–ion full cells were assembled using ICP-HC as the anode and $Na_3V_2(PO_4)_3$ (NVP) as the cathode denoted as NVP//ICP-HC (Figure 3g; Figures S18 and S19). Owing to the low-potential plateau of ICP-HC, the NVP//ICP-HC full cell exhibits a flat discharge plateau at approximately 3.3 V within 2.0–3.8 V and maintains well-defined voltage profiles from 0.1C to 5C (Figure 3h). Even at 5C, the cell delivers a reversible capacity of 96 mAh g^{-1} (based on the NVP cathode) and retains 95% of its initial capacity after 200 cycles at 1C, demonstrating favorable rate capability and cycling stability.

To quantify the full-cell-level benefit of ICP-HC, NVP//ISO-HC control cells were assembled under the same N/P ratio and testing conditions. NVP//ICP-HC achieves a higher energy density than NVP//ISO-HC, corresponding to an enhancement of approximately 12.7% (Figure S20 and Table S9). In addition, an anode mass normalized theoretical energy density analysis was performed by coupling the hard carbon anode profiles with an idealized 3.4 V NVP cathode plateau. This analysis further confirms that the enlarged low-voltage plateau of ICP-HC can more effectively contribute to full-cell output (Figure S21). Overall, these results demonstrate that the interconnected closed-pore architecture of ICP-HC can translate its enlarged low-voltage capacity and improved ion accessibility into enhanced full-cell output.

2.4 | Elucidation of the Sodium Storage Mechanism

To uncover the origin of the improved performance of ICP-HC, comprehensive operando/in situ techniques were employed, including operando XRD, operando Raman spectroscopy and in situ electrochemical impedance spectroscopy (EIS).

Operando XRD results for initial cycle reveal that both ISO-HC and ICP-HC shared high consistency in the long-range structural response and no distinct shift was observed for (002) peak during the overall discharge/charge process, indicating that no obvious sodium intercalation reaction occurred (Figure 4a,b; Figures S22 and 23). And operando Raman spectroscopy also displays similar identical spectral evolution for both ISO-HC and ICP-HC, indicating analogous sodium storage mechanisms (Figures 4c–f and S23). Specifically, during the initial sodiation stage (sloping region), the *D*-band (~1350 cm^{-1}) intensity decreases markedly, reflecting the preferential interaction of Na^+ with high-energy

15214095, 0, Downloaded from https://advanced.onlinelibrary.wiley.com/doi/10.1002/adma.74503 by University Town Of Shenzhen, Wiley Online Library on [08/09/2026]. See the Terms and Conditions (https://onlinelibrary.wiley.com/terms-and-conditions) on Wiley Online Library for rules of use; OA articles are governed by the applicable Creative Commons License

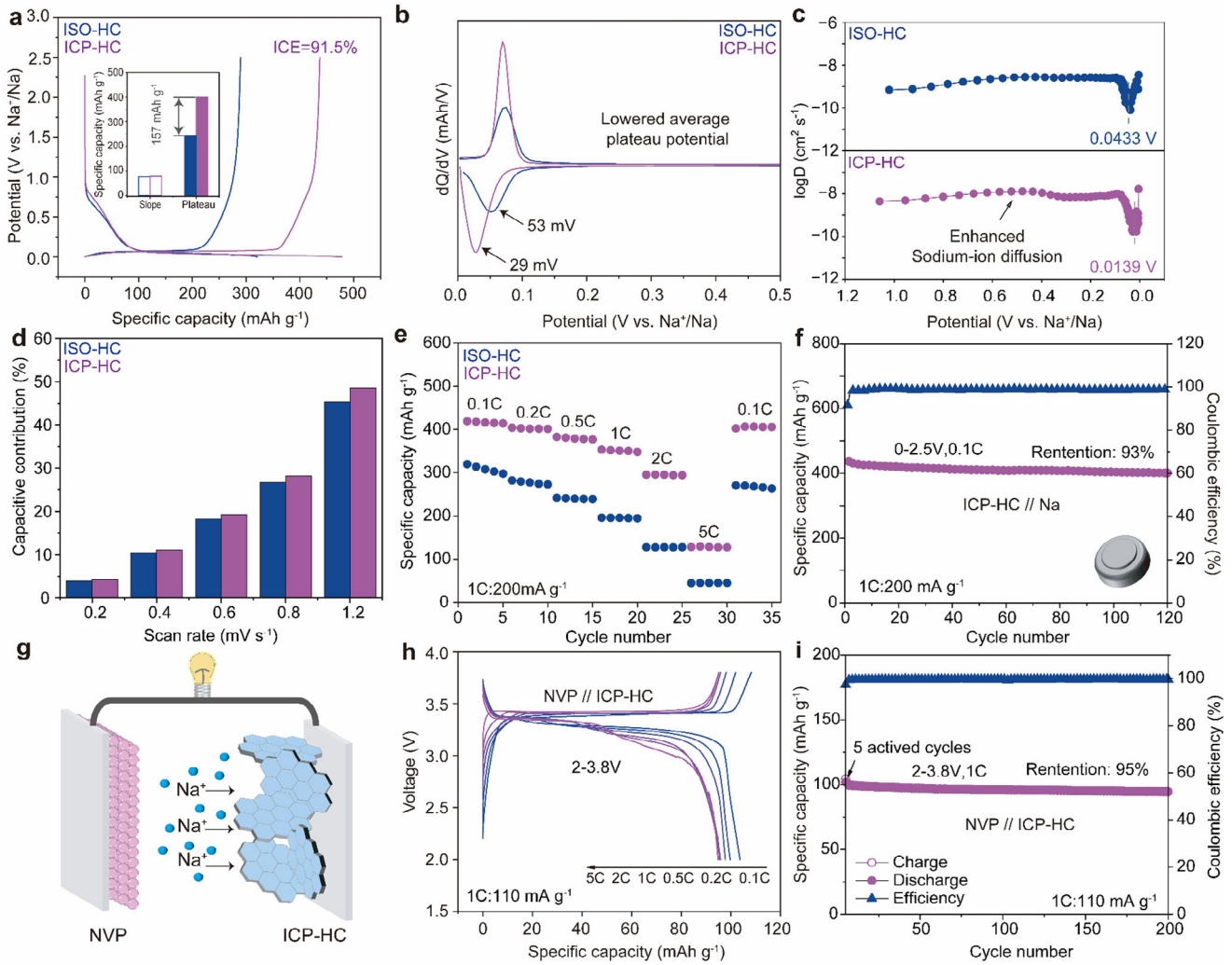


FIGURE 3 | Electrochemical sodium storage performance and kinetic analysis of the hard carbon anodes. (a) Galvanostatic charge–discharge (GCD) profiles of ISO-HC and ICP-HC at a current density of 20 mA g^{-1}, the insets display the quantitative comparison of capacity contributions (slope vs. plateau). (b) Differential capacity plots derived from the initial GCD curves, highlighting the lower plateau potential of ICP-HC. (c) Galvanostatic intermittent titration technique (GITT) calculated sodium ion diffusion coefficients. (d) Capacitive contribution at various scan rates ranging from 0.2 to 1.2 mV s^{-1}. (e) Rate capabilities evaluated at current densities from 0.1C to 5C. (f) Long-term cycling stability and Coulombic efficiency over 120 cycles in half-cell. (g) The schematic illustration of the full-cell configuration, where the ICP-HC anode is coupled with the $Na_3V_2(PO_4)_3$ cathode. (h) Charge/discharge curves of NVP//ICP-HC SIBs at various current densities. (i) Cycling performance of NVP//ICP-HC SIBs at a current density of 1C.

defect sites. Concurrently, the *G*-band undergoes a pronounced redshift from ~1580 to ~1540 cm^{-1}, which is attributed to charge transfer into the antibonding orbitals of the carbon lattice [48]. Notably, the *G*-band position remains essentially constant below 0.1 V, indicating saturation of electronic structure modulation and a transition of the Na storage mechanism from defect adsorption to pore filling. In this low-voltage region, sodium clusters accumulate within closed micropores, consistent with the widely reported pore-filling mechanism in hard carbon anodes [14, 15, 28, 48]. Upon desodiation, the reversible recovery of both the *G*-band position and *D*-band intensity confirms that this adsorption-filling process does not induce irreversible damage to the carbon framework.

To describe the kinetic evolution of these electrochemical processes, in situ EIS tests were performed, and the results are shown in Figure S24, the highly consistent impedance evolution trends observed for both ICP-HC and ISO-HC confirm that they share an identical fundamental sodium storage mechanism. Furthermore, model-independent distribution of relaxation times (DRT) analysis [49–52], transforming impedance spectra into discrete relaxation processes, were further employed. The DRT heatmaps reveal a stark contrast in transport kinetics (Figure 4g,h and Table S6). For ISO-HC, distinct high-intensity zones dominate the medium-frequency (τ_3-τ_4) and low-frequency (τ_5) ranges during the plateau stage, signifying severe kinetic barriers associated with charge transfer and restricted Na^+ diffusion into isolated voids. In sharp contrast, ICP-HC exhibits a significantly suppressed impedance response in these identical regions. This kinetic enhancement intrinsically stems from the highly interconnected and accessible pore network, which effectively eliminates diffusion bottlenecks and provides smoothed

15214095, 0, Downloaded from https://advanced.onlinelibrary.wiley.com/doi/10.1002/adma.74503 by University Town Of Shenzhen, Wiley Online Library on [08/09/2026]. See the Terms and Conditions (https://onlinelibrary.wiley.com/terms-and-conditions) on Wiley Online Library for rules of use; OA articles are governed by the applicable Creative Commons License

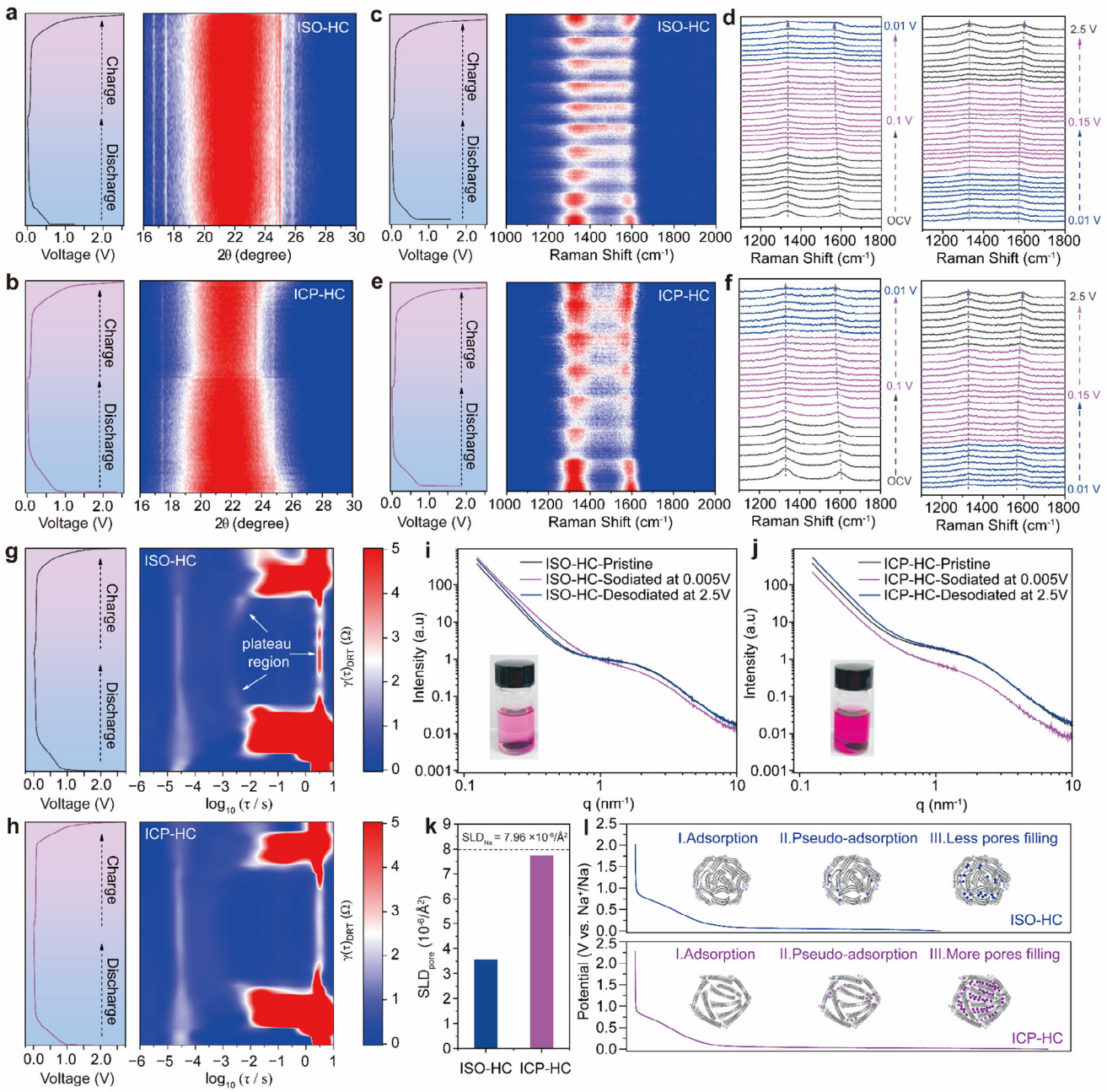


FIGURE 4 | Operando spectroscopic and structural investigation of the sodium storage mechanism. Operando XRD patterns and corresponding GCD profiles for (a) ISO-HC and (b) ICP-HC. Operando Raman spectra and corresponding GCD profiles for (c, d) ISO-HC and (e, f) ICP-HC. Distribution of relaxation times (DRT) heatmaps for (g) ISO-HC and (h) ICP-HC. Quantitative validation of pore filling: SAXS curves of pristine, fully sodiated (0.005 V), and desodiated (2.5 V) states for (i) ISO-HC and (j) ICP-HC. Inserts are digital photographs of the corresponding chemical titration with ethanol/phenolphthalein. (k) Comparison of the fitted scattering length density (SLD) of pores in the fully sodiated state. (l) Schematic illustration of the proposed sodium storage mechanism.

pathways for rapid sodium insertion into the deep internal voids (Figure S25 and Table S7).

Furthermore, to quantitatively assess pore utilization efficiency and the physicochemical state of the stored sodium, chemical titration coupled with ex situ small-angle X-ray scattering were employed. The SAXS profiles (Figure 4i,j) of both fully desodiated HCs (charged to 2.5 V) perfectly overlap with their pristine states, reaffirming the structural robustness of the carbon frameworks. Upon full sodiation (0.005 V), a pronounced structural evolution is observed, manifested by a substantial decrease in the low-q scattering intensity. This behavior originates from the reduced electron density contrast ($\Delta\rho$) between the carbon matrix and the internal pores, indicating effective Na infiltration. By extracting the pore scattering length density (SLD) through model fitting [15], the profound impact of pore accessibility is explicitly revealed. The ISO-HC sample exhibits only a modest SLD increase, indicative of partial pore filling and severe underutilization caused by restricted internal accessibility. Conversely, the pore SLD of the fully sodiated ICP-HC sharply

15214095, 0, Downloaded from https://advanced.onlinelibrary.wiley.com/doi/10.1002/adma.74503 by University Town Of Shenzhen, Wiley Online Library on [08/09/2026]. See the Terms and Conditions (https://onlinelibrary.wiley.com/terms-and-conditions) on Wiley Online Library for rules of use; OA articles are governed by the applicable Creative Commons License

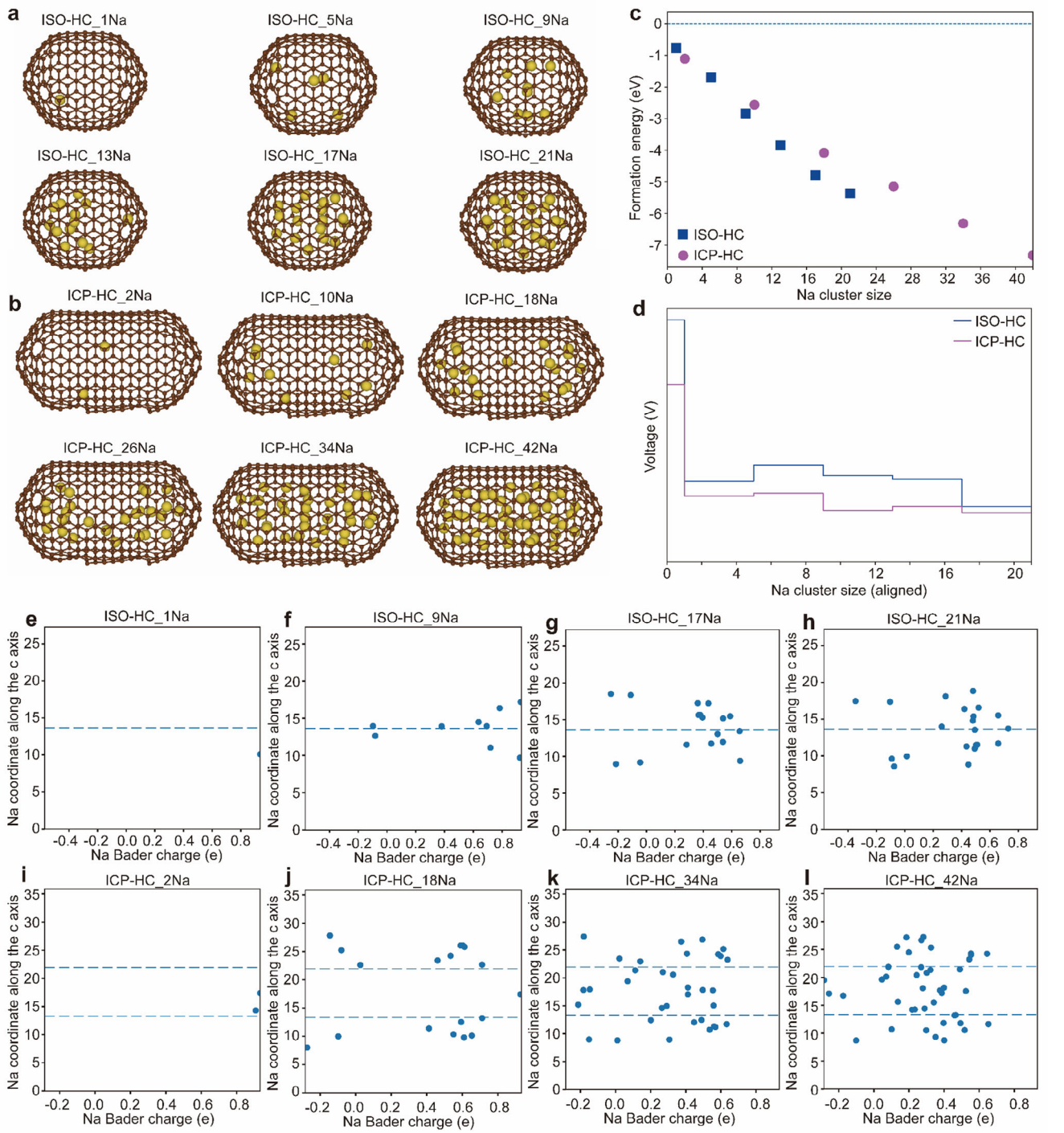


FIGURE 5 | DFT and MLIP theoretical simulations. Optimized structural models of sodiated: (a) ISO-HC and (b) ICP-HC. (c) Formation energy and (d) simulated voltage plateau profiles versus Na cluster size. Quantitative Bader charge analysis showing the electronic state transition of Na atoms during the progressive pore-filling process for the (e–h) ISO-HC and (i–l) ICP-HC models.

increases to approach the theoretical value of metallic sodium (Figure 4k). This atomic-scale evidence unambiguously proves that the expanded fused voids are highly accessible and densely occupied by sodium.

This maximized pore utilization is further corroborated by chemical titration (insets in Figure 4i,j, the electrodes contain the same mass of active material), which visually and quantitatively confirms that ICP-HC accommodates a substantially larger mass of electrochemically active sodium at 0.005 V than ISO-HC. The strong congruence between the elevated SLD values and the titration results demonstrates that the interconnected closed pores in ICP-HC function not merely as isolated voids, but as highly accessible reservoirs for the dense accumulation of multilayer quasi-metallic sodium clusters. As conceptually summarized in the proposed sodium storage mechanism (Figure 4l), while both ISO-HC and ICP-HC undergo similar surface adsorption (I) and pseudo-adsorption (II) stages within the high-voltage

15214095, 0, Downloaded from https://advanced.onlinelibrary.wiley.com/doi/10.1002/adma.74503 by University Town Of Shenzhen, Wiley Online Library on [08/09/2026]. See the Terms and Conditions (https://onlinelibrary.wiley.com/terms-and-conditions) on Wiley Online Library for rules of use; OA articles are governed by the applicable Creative Commons License

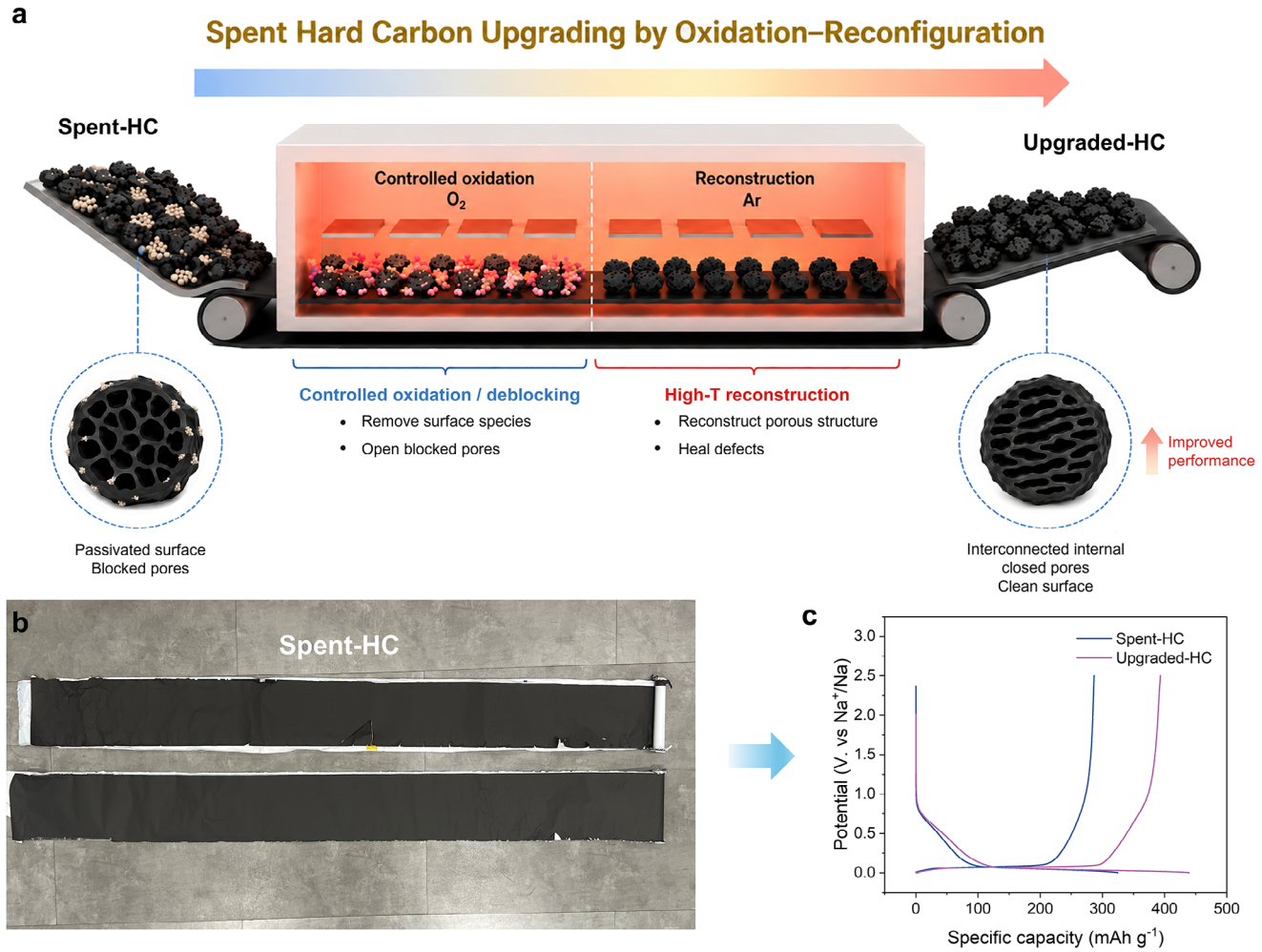


FIGURE 6 | Proof-of-concept upgrading of spent hard-carbon anodes by the oxidation–reconfiguration strategy. (a) Schematic of spent-HC upgradation through oxidation–reconfiguration method. (b) Optical image of spent-HC. (c) Initial charge–discharge curves for spent-HC and upgraded spent-HC.

sloping region, their low-voltage pore-filling behaviors (III) diverge drastically. Unlike the restricted ce between the elng″ state in ISO-HC caused by isolated dead pores, the interconnected closed pore network of ICP-HC permits massive and continuous sodium cluster accommodation (more pores filling). Consequently, the oxidation-reconfiguration strategy successfully completely unlocks the internal pore volume, simultaneously maximizing the pore utilization efficiency and lowering the nucleation barrier for sodium clustering, thereby fundamentally accounting for the ultra-high plateau capacity and excellent rate performance of ICP-HC.

To theoretically elucidate the thermodynamic origins of the ultra-high plateau capacity and the atomistic mechanism of Na storage, density functional theory (DFT) coupled with machine learning interatomic potentials (MLIP) was employed [53–56]. To construct the fine-tuning dataset, a variable number of Na atoms were randomly inserted into ISO-HC and ICP-HC structures. Initial structural relaxations were performed using the pre-trained MACE-OMAT-0 [57] model, and all intermediate configurations from the relaxation trajectories were collected. From this pool, 97 representative structures were selected using farthest-point sampling [58] based on NEP [59] descriptors. These structures were partitioned into training, validation, and test sets in an 8:1:1 ratio. Density Functional Theory (DFT) calculations were carried out using the ABACUS [56] software package. To facilitate model convergence and reduce learning complexity, configurations exhibiting any force component exceeding 50 eV/Å were excluded from the dataset. The model was subsequently fine-tuned on this curated dataset for 30 epochs. The performance of the fine-tuned model across the training, validation, and test sets is illustrated in Figure S26. Furthermore, Capped carbon nanotube models were constructed to represent the closed-pore architectures of ISO-HC and ICP-HC as shown in Figure S27. Both models possess an identical diameter of 13.6 Å, but the ICP-HC model extends to ~18.5 Å in length, nearly twice that of the ISO-HC model (~10 Å). This specific geometric design explicitly simulates the structural evolution induced by the oxidation-reconfiguration strategy; wherein adjacent isolated voids progressively merge into an expanded, unified closed pore. To maintain a consistent defect density, one and two single-vacancy defects were incorporated into the ISO-HC and ICP-HC models, respectively, which subsequently reconstructed into stable pentagon-nonagon pairs following DFT relaxation.

15214095, 0, Downloaded from https://advanced.onlinelibrary.wiley.com/doi/10.1002/adma.74503 by University Town Of Shenzhen, Wiley Online Library on [08/09/2026]. See the Terms and Conditions (https://onlinelibrary.wiley.com/terms-and-conditions) on Wiley Online Library for rules of use; OA articles are governed by the applicable Creative Commons License

Following the progressive random insertion and global optimization of Na atoms, Unlike the confined ISO-HC model where severe steric hindrance restricts Na clustering (Figure 5a), the interconnected pore network of ICP-HC (Figure 5b) facilitates the continuous accommodation of large, densely packed quasi-metallic Na clusters. Furthermore, the formation energies and corresponding voltage profiles were extracted to evaluate the sodiation thermodynamics (Figure 5c,d). Strikingly, the expanded ICP-HC model exhibits a much earlier onset of the low-voltage plateau region. The simulated sodiation potential of ICP-HC drops to approximately 0.1 V upon the insertion of merely 9 equivalent Na atoms, whereas the confined ISO-HC model requires 17 equivalent Na atoms to reach this critical threshold. Furthermore, the voltage profile of ICP-HC remains consistently lower throughout the entire pore-filling process, thermodynamically validating its capability to deliver a significantly higher plateau capacity. The atomistic Na-filling behavior elucidates this enhancement: Na atoms initially adsorb at high-curvature capped regions and defect sites before aggregating into clusters. In the ICP-HC model, the expanded internal volume between the dual defect sites accommodates the simultaneous growth and eventual merging of multiple Na clusters. This spatial advantage fundamentally mitigates steric hindrance, facilitating the formation of larger, densely packed Na clusters. Additionally, the reduced ratio of high-curvature surface area to total volume in ICP-HC minimizes high-energy binding sites, further promoting a faster transition into the plateau region.

To quantitatively monitor the electronic state transition of Na during cluster growth, Bader charge analysis was systematically performed (Figure 5e–l). At low sodiation stages, Na atoms predominantly exhibit Bader charges near +1e, characteristic of ionic adsorption corresponding to the sloping capacity. As the internal pore filling proceeds, the proportion of Na atoms displaying quasi-metallic character (< +0.5e) substantially increases. When comparing both models at an equivalent sodiation state (e.g., 21 inserted Na atoms), the ICP-HC model yields 17.5 equivalent metallic Na atoms, which is noticeably higher than the 15 atoms observed in ISO-HC. This quantitative charge distribution reveals that metallic Na emerges earlier and forms more extensive clusters within the ICP-HC framework. Collectively, these theoretical findings provide compelling evidence that the expanded and fused closed-pore architecture, constructed via the oxidation-reconfiguration strategy, intrinsically lowers the nucleation barrier for quasi-metallic Na. This atomistic mechanism underpins the ultra-high plateau capacity observed in the electrochemical evaluations.

2.5 | Practical Extensibility of the Oxidation-Reconfiguration Strategy

To further verify its further practical application on spent-HC, we performed a proof-of-concept experiment using spent-HC collected from cylindrical cells after cycling. As shown in Figure 6a, the spent-HC contains passivated surface and blocked pores after repeated electrochemical operation. Through controlled oxidative deblocking followed by high-temperature reconstruction, the upgraded-HC recovers with cleaner surfaces and reconfigured closed-pore structure. After the oxidation-reconfiguration treatment, the upgraded HC displays a pronounced low-voltage plateau and delivers a reversible capacity of approximately 400 mAh g^{-1} (Figure 6c), suggesting that this strategy can effectively improve electrochemical performance for spent hard-carbon anodes [1, 2, 60–62].

3 | Conclusions

In summary, we propose a potentially scalable oxidation-reconfiguration strategy to unlock the latent capacity of hard carbons. By precisely coupling mild oxidation (400°C) with high-temperature carbon layers rearrangement (1600°C), we engineered an interconnected closed-pore network. As corroborated by NPDF, operando techniques, SAXS, and DFT and MLIP simulations, this tailored structure effectively eliminates isolated voids to maximize internal pore accessibility. Consequently, it smooths kinetic pathways and significantly lowers the nucleation barrier for the dense accommodation of quasi-metallic sodium clusters, fundamentally driving the superior storage performance.

The optimized ICP-HC anode delivers a remarkable reversible capacity of 437 mAh g^{-1} alongside a high initial Coulombic efficiency of 91.5%. Most notably, by fundamentally breaking the conventional trade-off between high plateau capacity and sluggish kinetics, it simultaneously achieves an ultra-high discharge plateau capacity of 399 mAh g^{-1} and exceptional rate capability (300 mAh g^{-1} at 2C). The practical viability of this strategy is further robustly validated in an NVP//ICP-HC full cell, demonstrating outstanding rate performance (96 mAh g^{-1} at 5C based on NVP) and exceptional cycling stability with 95% capacity retention after 200 cycles at 1C. Furthermore, a proof-of-concept spent-HC upgrading test suggests the practical extensibility of this strategy, as the upgraded spent hard carbon improves a pronounced low-voltage plateau and reversible capacity.

Ultimately, this study provides fundamental insights into precise pore engineering and maximizing pores utilization efficiency. By establishing a facile and universal pathway to upgrade commercial carbons, this work breaks the capacity bottleneck of carbonaceous anodes, propelling the development of high-energy and long-life practical SIBs.

Acknowledgements

We gratefully acknowledge the financial support received from National Natural Science Foundation of China (grant number 92472206), National Center for International Research of Power Batteries and Materials (no. 2015B01015), Guangdong Key Laboratory of Design and Calculation of New Energy Materials (no. 2017B030301013), Shenzhen Key Laboratory of New Energy Resources Genome Preparation and Testing (no. ZDSYS201707281026184), and the Key Project of Basic Research of the Shenzhen Natural Science Foundation (JCYJ20241202125901003). We thank Shenzhen Guangming Science City Development and Construction Co., Ltd. and its Material Genome Big-Science Facilities Platform for providing technical support and assistance in data collection and analysis. Additionally, we thank the staff members of the Multi-Physics Instrument (https://cstr.cn/31113.02.CSNS.MPI) at the China Spallation Neutron Source (CSNS) (https://cstr.cn/31113.02.CSNS), for providing technical support and assistance in data collection and analysis.

15214095, 0, Downloaded from https://advanced.onlinelibrary.wiley.com/doi/10.1002/adma.74503 by University Town Of Shenzhen, Wiley Online Library on [08/09/2026]. See the Terms and Conditions (https://onlinelibrary.wiley.com/terms-and-conditions) on Wiley Online Library for rules of use; OA articles are governed by the applicable Creative Commons License

Conflicts of Interest

The authors declare no conflicts of interest.

Data Availability Statement

The data that support the findings of this study are available from the corresponding author upon reasonable request.

References

1. N. Yabuuchi, K. Kubota, M. Dahbi, and S. Komaba, "Research Development on Sodium-Ion Batteries," *Chemical Reviews* 114 (2014): 11636–11682.

2. J. Y. Hwang, S. T. Myung, and Y. K. Sun, "Sodium-Ion Batteries: Present and Future," *Chemical Society Reviews* 46 (2017): 3529–3614, https://doi.org/10.1039/C6CS00776G.

3. R. Usiskin, Y. Lu, J. Popovic, et al., "Fundamentals, Status and Promise of Sodium-Based Batteries," *Nature Reviews Materials* 6 (2021): 1020–1035, https://doi.org/10.1038/s41578-021-00324-w.

4. Y. Chu, J. Zhang, Y. Zhang, et al., "Reconfiguring Hard Carbons With Emerging Sodium-Ion Batteries: A Perspective," *Advanced Materials* 35 (2023): 2212186, https://doi.org/10.1002/adma.202212186.

5. X. Fan, X. Kong, P. Zhang, and J. Wang, "Research Progress on Hard Carbon Materials in Advanced Sodium-Ion Batteries," *Energy Storage Materials* 69 (2024): 103386, https://doi.org/10.1016/j.ensm.2024.103386.

6. X. Dou, I. Hasa, D. Saurel, et al., "Hard Carbons for Sodium-Ion Batteries: Structure, Analysis, Sustainability, and Electrochemistry," *Materials Today* 23 (2019): 87–104, https://doi.org/10.1016/j.mattod.2018.12.040.

7. B. Pei, H. Yu, L. Zhang, et al., "Hard Carbon for Sodium-Ion Batteries: From Fundamental Research to Practical Applications," *Advanced Materials* 37 (2025): 2504574, https://doi.org/10.1002/adma.202504574.

8. F. Xie, Z. Xu, Z. Guo, and M.-M. Titirici, "Hard Carbons for Sodium-Ion Batteries and Beyond," *Progress in Energy* 2 (2020): 042002, https://doi.org/10.1088/2516-1083/aba5f5.

9. Q. Meng, Y. Lu, F. Ding, Q. Zhang, L. Chen, and Y.-S. Hu, "Tuning the Closed Pore Structure of Hard Carbons With the Highest Na Storage Capacity," *ACS Energy Letters* 4 (2019): 2608–2612, https://doi.org/10.1021/acsenergylett.9b01900.

10. A. Bauer, J. Song, S. Vail, W. Pan, J. Barker, and Y. Lu, "The Scale-Up and Commercialization of Nonaqueous Na-Ion Battery Technologies," *Advanced Energy Materials* 8 (2018): 1702869, https://doi.org/10.1002/aenm.201702869.

11. X. Zhang, X. Dong, X. Qiu, et al., "Extended Low-Voltage Plateau Capacity of Hard Carbon Spheres Anode for Sodium Ion Batteries," *Journal of Power Sources* 476 (2020): 228550, https://doi.org/10.1016/j.jpowsour.2020.228550.

12. J. M. Stratford, A. K. Kleppe, D. S. Keeble, et al., "Correlating Local Structure and Sodium Storage in Hard Carbon Anodes: Insights From Pair Distribution Function Analysis and Solid-State NMR," *Journal of the American Chemical Society* 143 (2021): 14274–14286, https://doi.org/10.1021/jacs.1c06058.

13. J. Wang, J. Liu, Y. Zhou, B. Zhao, H. Wang, and J. Li, "Toward the Design of High-Energy-Density Practical Sodium Pouch Cells," *Advanced Functional Materials* 35 (2025): 06670, https://doi.org/10.1002/adfm.202506670.

14. Q. Li, X. Liu, Y. Tao, et al., "Sieving Carbons Promise Practical Anodes With Extensible Low-Potential Plateaus for Sodium Batteries," *National Science Review* 9 (2022): nwac084, https://doi.org/10.1093/nsr/nwac084.

15. E. N. Antonio and T. D. Martinez, "Revealing the Sodium Storage Mechanisms in Hard Carbon Pores," *Advanced Energy Materials* 13 (2023): 2302171.

16. W. Zhang, Y. Du, Y. Qiu, et al., "Closed-Pore Engineering in Hard Carbon for Sodium Ion Storage: Advances, Challenges and Future Horizons," *Advanced Energy Materials* 15 (2025): 03884, https://doi.org/10.1002/aenm.202503884.

17. D. Igarashi, Y. Tanaka, K. Kubota, et al., "New Template Synthesis of Anomalously Large Capacity Hard Carbon for Na- and K-Ion Batteries," *Advanced Energy Materials* 13 (2023): 2302647, https://doi.org/10.1002/aenm.202302647.

18. A. Kamiyama, K. Kubota, D. Igarashi, et al., "MgO-Template Synthesis of Extremely High Capacity Hard Carbon for Na-Ion Battery," *Angewandte Chemie International Edition* 60 (2021): 5114–5120, https://doi.org/10.1002/anie.202013951.

19. Z. Lu, J. Wang, W. Feng, et al., "Zinc Single-Atom-Regulated Hard Carbons for High-Rate and Low-Temperature Sodium-Ion Batteries," *Advanced Materials* 35 (2023): 2211461, https://doi.org/10.1002/adma.202211461.

20. K. Wang, F. Sun, H. Wang, et al., "Altering Thermal Transformation Pathway to Create Closed Pores in Coal-Derived Hard Carbon and Boosting of Na + Plateau Storage for High-Performance Sodium-Ion Battery and Sodium-Ion Capacitor," *Advanced Functional Materials* 32 (2022): 2203725, https://doi.org/10.1002/adfm.202203725.

21. X. Yin, Z. Lu, J. Wang, et al., "Enabling Fast Na + Transfer Kinetics in the Whole-Voltage-Region of Hard-Carbon Anodes for Ultrahigh-Rate Sodium Storage," *Advanced Materials* 34 (2022): 2109282, https://doi.org/10.1002/adma.202109282.

22. F. Yuan, D. Zhang, Z. Li, et al., "Unraveling the Intercorrelation Between Micro/Mesopores and K Migration Behavior in Hard Carbon," *Small* 18 (2022): 2107113, https://doi.org/10.1002/smll.202107113.

23. C. Bommier, X. Ji, and P. A. Greaney, "Electrochemical Properties and Theoretical Capacity for Sodium Storage in Hard Carbon: Insights From First Principles Calculations," *Chemistry of Materials* 31 (2018): 658–677, https://doi.org/10.1021/acs.chemmater.8b01390.

24. Y. Li, Y. Lu, Q. Meng, et al., "Regulating Pore Structure of Hierarchical Porous Waste Cork-Derived Hard Carbon Anode for Enhanced Na Storage Performance," *Advanced Energy Materials* 9 (2019): 1902852, https://doi.org/10.1002/aenm.201902852.

25. X. Zhang, Y. Cao, G. Li, et al., "Exploring Carbonization Temperature to Create Closed Pores for Hard Carbon as High-Performance Sodium-Ion Battery Anodes," *Small* 20 (2024): 2311197, https://doi.org/10.1002/smll.202311197.

26. N. Sun, Z. Guan, Y. Liu, et al., "Extended "Adsorption–Insertion" Model: A New Insight Into the Sodium Storage Mechanism of Hard Carbons," *Advanced Energy Materials* 9 (2019): 1901351, https://doi.org/10.1002/aenm.201901351.

27. Y. V. Butenko, S. Krishnamurthy, A. K. Chakraborty, et al., "Photoemission Study of Onionlike Carbons Produced by Annealing Nanodiamonds," *Physical Review B* 71 (2005): 075420, https://doi.org/10.1103/PhysRevB.71.075420.

28. J. C. Hyun, H. M. Jin, J. H. Kwak, et al., "Design Guidelines for a High-Performance Hard Carbon Anode in Sodium Ion Batteries," *Energy & Environmental Science* 17 (2024): 2856–2863, https://doi.org/10.1039/D4EE00315B.

29. H. Au, H. Alptekin, A. C. S. Jensen, et al., "A Revised Mechanistic Model for Sodium Insertion in Hard Carbons," *Energy & Environmental Science* 13 (2020): 3469–3479, https://doi.org/10.1039/D0EE01363C.

30. A. Gomez-Martin, J. Martinez-Fernandez, M. Ruttert, M. Winter, T. Placke, and J. Ramirez-Rico, "Correlation of Structure and Performance of Hard Carbons as Anodes for Sodium Ion Batteries," *Chemistry of Materials* 31 (2019): 7288–7299, https://doi.org/10.1021/acs.chemmater.9b01768.

31. A. K. Ladavos, A. P. Katsoulidis, A. Iosifidis, K. S. Triantafyllidis, T. J. Pinnavaia, and P. J. Pomonis, "The BET Equation, the Inflection Points of N2 Adsorption Isotherms and the Estimation of Specific Surface Area of Porous Solids," *Microporous and Mesoporous Materials* 151 (2012): 126–133, https://doi.org/10.1016/j.micromeso.2011.11.005.

15214095, 0, Downloaded from https://advanced.onlinelibrary.wiley.com/doi/10.1002/adma.74503 by University Town Of Shenzhen, Wiley Online Library on [08/09/2026]. See the Terms and Conditions (https://onlinelibrary.wiley.com/terms-and-conditions) on Wiley Online Library for rules of use; OA articles are governed by the applicable Creative Commons License

32. M. Thommes, K. Kaneko, A. V. Neimark, et al., "Physisorption of Gases, With Special Reference to the Evaluation of Surface Area and Pore Size Distribution (IUPAC Technical Report)," *Pure and Applied Chemistry* 87 (2015): 1051–1069, https://doi.org/10.1515/pac-2014-1117.

33. H. Rennhofer, J. Köhnke, J. Keckes, et al., "Pore Development During the Carbonization Process of Lignin Microparticles Investigated by Small Angle X-Ray Scattering," *Molecules* 26 (2021): 2087, https://doi.org/10.3390/molecules26072087.

34. R. Diduszko, A. Swiatkowski, and B. J. Trznadel, "On Surface of Micropores and Fractal Dimension of Activated Carbon Determined on the Basis of Adsorption and SAXS Investigations," *Carbon* 38 (2000): 1153–1162, https://doi.org/10.1016/S0008-6223(99)00236-5.

35. Y. W. Zeng, P. Riello, A. Benedetti, and G. Fagherazzi, "Fractal Model of Amorphous and Semicrystalline Nano-Sized Zirconia Aerogels," *Journal of Non-Crystalline Solids* 185 (1995): 78–83, https://doi.org/10.1016/0022-3093(94)00678-4.

36. D. Saurel, J. Segalini, M. Jauregui, et al., "A SAXS Outlook on Disordered Carbonaceous Materials for Electrochemical Energy Storage," *Energy Storage Materials* 21 (2019): 162–173, https://doi.org/10.1016/j.ensm.2019.05.007.

37. D. Franke and D. I. Svergun, "DAMMIF, A Program for Rapid Ab-Initio Shape Determination in Small-Angle Scattering," *Journal of Applied Crystallography* 42 (2009): 342–346, https://doi.org/10.1107/S0021889809000338.

38. M. V. Petoukhov and D. I. Svergun, "Ambiguity Assessment of Small-Angle Scattering Curves From Monodisperse Systems," *Acta Crystallographica Section D Biological Crystallography* 71 (2015): 1051–1058, https://doi.org/10.1107/S1399004715002576.

39. A. T. Tuukkanen, G. J. Kleywegt, and D. I. Svergun, "Resolution of Ab Initio Shapes Determined From Small-Angle Scattering," *International Union of Crystallography Journal* 3 (2016): 440–447, https://doi.org/10.1107/S2052252516016018.

40. V. V. Volkov and D. I. Svergun, "Uniqueness of Ab Initio Shape Determination in Small-Angle Scattering," *Journal of Applied Crystallography* 36 (2003): 860–864, https://doi.org/10.1107/S0021889803000268.

41. H. Yamamoto, S. Muratsubaki, K. Kubota, et al., "Synthesizing Higher-Capacity Hard-Carbons From Cellulose for Na- and K-Ion Batteries," *Journal of Materials Chemistry A* 6 (2018): 16844–16848, https://doi.org/10.1039/C8TA05203D.

42. P. Huang, Z. Guo, Z. Li, et al., "Spatiotemporal Evolution in Hard Carbon Synthesis via Electrothermal Coupling Strategy for High-Performance Sodium-Ion Batteries," *Advanced Materials* 37 (2025): 2507521, https://doi.org/10.1002/adma.202507521.

43. Y. Jiang and J. Liu, "Definitions of Pseudocapacitive Materials: A Brief Review," *Energy & Environmental Materials* 2 (2019): 30–37, https://doi.org/10.1002/eem2.12028.

44. J. Liu, J. Wang, C. Xu, et al., "Advanced Energy Storage Devices: Basic Principles, Analytical Methods, and Rational Materials Design," *Advanced Science* 5 (2018): 1700322, https://doi.org/10.1002/advs.201700322.

45. Q. Chen, Q. Wen, C. Li, et al., "High-Compaction Spherical Carbon With Tunable Rich Pore Structures for Efficient Sodium Storage," *Advanced Materials* 38 (2026): 15495, https://doi.org/10.1002/adma.202515495.

46. W. Huang, C. Wu, L. Zhong, et al., "Unlocking Kinetic Limitations in Hard-Carbon Anodes to Enable Practical Fast-Charging Sodium-Ion Batteries," *Advanced Energy Materials* 16 (2026): 05568, https://doi.org/10.1002/aenm.202505568.

47. C. Li, Q. Chen, Y. Zhang, et al., "Molecular Reconfiguration of Pitch-Derived Hard Carbon Anodes With Balanced Thermodynamic Stability and Rapid Sodium Storage Kinetics for High-Performance Sodium-Ion Batteries," *Energy Storage Materials* 82 (2025): 104580, https://doi.org/10.1016/j.ensm.2025.104580.

48. E. O. Eren, E. Senokos, E. Scoppola, Z. Song, M. Antonietti, and P. Giusto, "An Enhanced Three-Stage Model for Sodium Storage in Hard Carbons," *Energy & Environmental Science* 18 (2025): 7859–7868, https://doi.org/10.1039/D4EE06029F.

49. J. Chen, E. Quattrocchi, F. Ciucci, and Y. Chen, "Charging Processes in Lithium-Oxygen Batteries Unraveled Through the Lens of the Distribution of Relaxation Times," *Chemistry* 9 (2023): 2267–2281, https://doi.org/10.1016/j.chempr.2023.04.022.

50. Y. Lu, C.-Z. Zhao, J.-Q. Huang, and Q. Zhang, "The Timescale Identification Decoupling Complicated Kinetic Processes in Lithium Batteries," *Joule* 6 (2022): 1172–1198, https://doi.org/10.1016/j.joule.2022.05.005.

51. T. H. Wan, M. Saccoccio, C. Chen, and F. Ciucci, "Influence of the Discretization Methods on the Distribution of Relaxation Times Deconvolution: Implementing Radial Basis Functions With DRTtools," *Electrochimica Acta* 184 (2015): 483–499, https://doi.org/10.1016/j.electacta.2015.09.097.

52. A. Weiß, S. Schindler, S. Galbiati, et al., "Distribution of Relaxation Times Analysis of High-Temperature PEM Fuel Cell Impedance Spectra," *Electrochimica Acta* 230 (2017): 391–398.

53. P. Li, X. Liu, M. Chen, et al., "Large-Scale Ab Initio Simulations Based on Systematically Improvable Atomic Basis," *Computational Materials Science* 112 (2016): 503–517, https://doi.org/10.1016/j.commatsci.2015.07.004.

54. J. Moellmann and S. Grimme, "DFT-D3 Study of some Molecular Crystals," *Journal of Physical Chemistry C* 118 (2014): 7615–7621, https://doi.org/10.1021/jp501237c.

55. H. Yu, Z. Yi, W. Jia, et al., "Confinement-Induced Stability Evolution of Na Clusters in Closed Pores of Hard Carbon: A DFT and AIMD Study," *Journal of Physical Chemistry A* 129 (2025): 3231–3241, https://doi.org/10.1021/acs.jpca.5c00209.

56. W. Zhou, D. Zheng, Q. Liu, et al., "ABACUS: An Electronic Structure Analysis Package for the AI Era," *Journal of Chemical Physics* 163 (2025): 192501, https://doi.org/10.1063/5.0297563.

57. I. Batatia, P. Benner, Y. Chiang, et al., "A Foundation Model for Atomistic Materials Chemistry," *Journal of Chemical Physics* 163 (2025): 184110, https://doi.org/10.1063/5.0297006.

58. A. P. Bartók, S. De, C. Poelking, et al., "Machine Learning Unifies the Modeling of Materials and Molecules," *Science Advances* 3 (2017): 1701816, https://doi.org/10.1126/sciadv.1701816.

59. K. Xu, H. Bu, S. Pan, et al., "GPUMD 4.0: A High-Performance Molecular Dynamics Package for Versatile Materials Simulations With Machine-Learned Potentials," *Materials Genome Engineering Advances* 3 (2025): 70028, https://doi.org/10.1002/mgea.70028.

60. S. Mariyappan, P. Desai, M. Morcrette, and J.-M. Tarascon, "From Lab to Market With Sustainable Sodium-Ion Batteries," *Nature Sustainability* 9 (2026): 360–371, https://doi.org/10.1038/s41893-025-01701-x.

61. Q. Wen, C. Li, Q. Chen, et al., "Carbon Engineering for Sodium Batteries: Multi-Role Architectures Bridging Material Design and Hybrid System Innovation," *Chemical Society Reviews* 54 (2025): 9317–9369, https://doi.org/10.1039/D5CS00515A.

62. W. Zuo, Z. Liu, A. Dopilka, et al., "Next-Generation Anodes for High-Energy and Low-Cost Sodium-Ion Batteries," *Nature Reviews Materials* 11 (2026): 117–135, https://doi.org/10.1038/s41578-025-00857-4.

Supporting Information

Additional supporting information can be found online in the Supporting Information section.

Supporting File: adma74503-sup-0001-SuppMat.docx.

15214095, 0, Downloaded from https://advanced.onlinelibrary.wiley.com/doi/10.1002/adma.74503 by University Town Of Shenzhen, Wiley Online Library on [08/09/2026]. See the Terms and Conditions (https://onlinelibrary.wiley.com/terms-and-conditions) on Wiley Online Library for rules of use; OA articles are governed by the applicable Creative Commons License